

This is a repository copy of *In situ x-ray* computed tomography of zinc—air primary cells during discharge: correlating discharge rate to anode morphology.

White Rose Research Online URL for this paper: <a href="https://eprints.whiterose.ac.uk/id/eprint/233269/">https://eprints.whiterose.ac.uk/id/eprint/233269/</a>

Version: Published Version

## Article:

Hack, J. orcid.org/0000-0002-5529-4750, Patel, D. orcid.org/0000-0003-4288-2825, Bailey, J.J. orcid.org/0000-0003-2397-6690 et al. (3 more authors) (2022) In situ x-ray computed tomography of zinc—air primary cells during discharge: correlating discharge rate to anode morphology. Journal of Physics: Materials, 5 (1). 014001. ISSN: 2515-7639

https://doi.org/10.1088/2515-7639/ac3f9a

## Reuse

This article is distributed under the terms of the Creative Commons Attribution (CC BY) licence. This licence allows you to distribute, remix, tweak, and build upon the work, even commercially, as long as you credit the authors for the original work. More information and the full terms of the licence here: https://creativecommons.org/licenses/

#### Takedown

If you consider content in White Rose Research Online to be in breach of UK law, please notify us by emailing eprints@whiterose.ac.uk including the URL of the record and the reason for the withdrawal request.





## **PAPER • OPEN ACCESS**

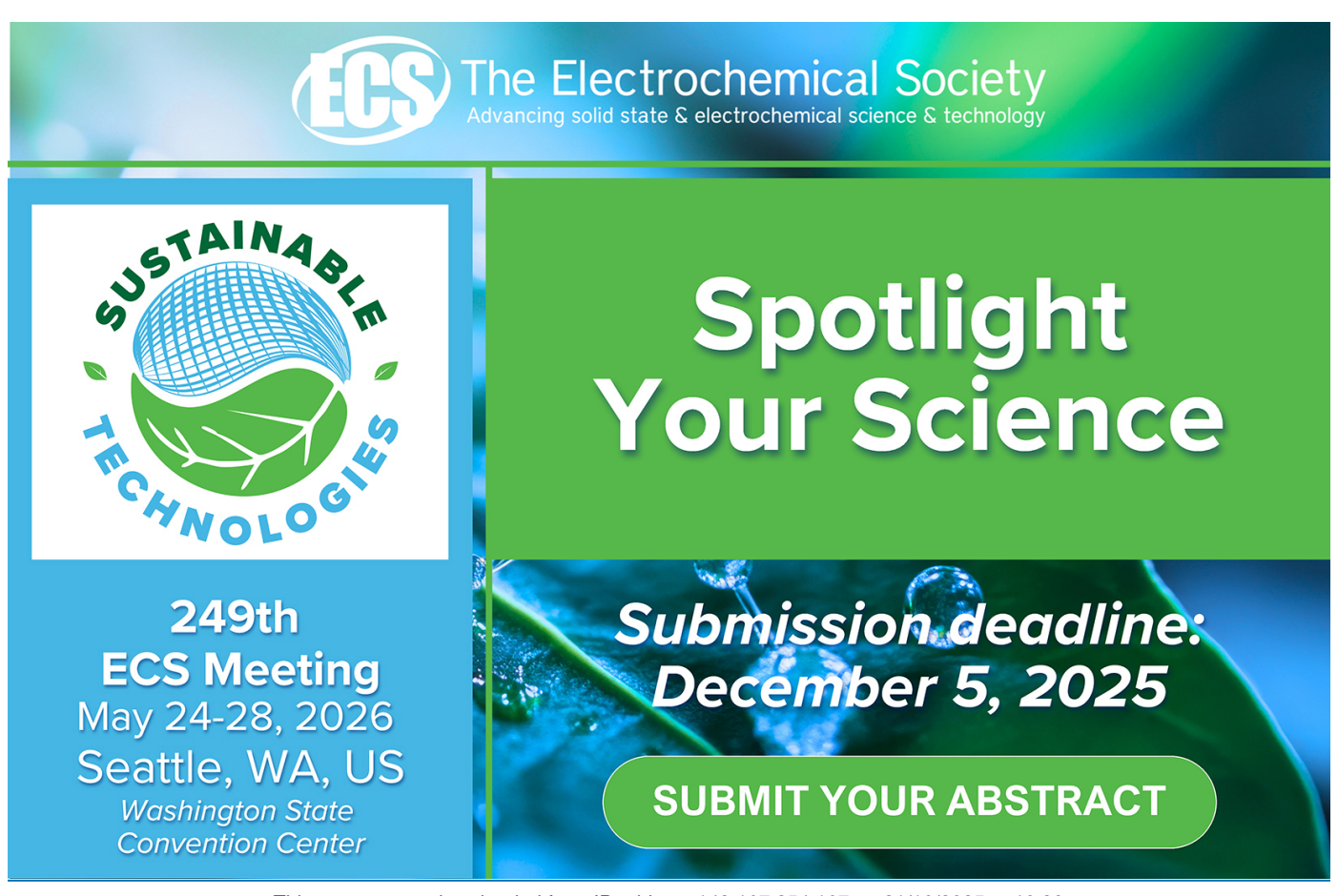
In situ x-ray computed tomography of zinc–air primary cells during discharge: correlating discharge rate to anode morphology

To cite this article: Jennifer Hack et al 2022 J. Phys. Mater. 5 014001

View the article online for updates and enhancements.

## You may also like

- High Performance Air Breathing Zinc-Air Battery with PtNi and PtCo Bifunctional Electrocatalyst on N Activated Mesoporous Carbon Prabakaran Varathan, Prabu Moni, Sumanta Kumar Das et al.
- Preparation and performance of low-cost and high-active transition metal alloy catalysts for improving the performance of zinc-air batteries Yige Wang
- Aquatic Colloidal Graphene Gel Polymer Electrolyte for Flexible Rechargeable Zinc Air Batteries Xingliang Jia, Jingling Ma, Liangliang Zhang et al.



## Journal of Physics: Materials



#### **OPEN ACCESS**

#### RECEIVED

11 October 2021

#### REVISED

19 November 2021

## ACCEPTED FOR PUBLICATION

2 December 2021

#### PUBLISHED

17 December 2021

Original content from this work may be used under the terms of the Creative Commons Attribution 4.0 licence.

Any further distribution of this work must maintain attribution to the author(s) and the title of the work, journal citation and DOI.



#### **PAPER**

# *In situ* x-ray computed tomography of zinc–air primary cells during discharge: correlating discharge rate to anode morphology

Jennifer Hack<sup>1,\*</sup>, Drasti Patel<sup>1</sup>, Josh J Bailey<sup>1,2</sup>, Francesco Iacoviello<sup>1</sup>, Paul R Shearing<sup>1,3</sup> and Dan J L Brett<sup>1,3,\*</sup>

- <sup>1</sup> Electrochemical Innovation Lab, Department of Chemical Engineering, University College London, London WC1E 7JE, United Kingdom
- School of Mechanical and Aerospace Engineering, Queen's University Belfast, Stranmillis Road, Belfast, BT9 5AH, United Kingdom
- The Faraday Institution, Quad One, Becquerel Avenue, Harwell Campus, Didcot OX11 0RA, United Kingdom
- \* Authors to whom any correspondence should be addressed.

E-mail: jennifer.hack.16@ucl.ac.uk and d.brett@ucl.ac.uk

Keywords: zinc-air cells, x-ray computed tomography, in-situ imaging, correlative imaging

Supplementary material for this article is available online

#### **Abstract**

Zinc-air batteries have gained significant attention as safe battery alternatives, with high theoretical energy densities and a high abundance of their constituent materials. However, barriers to their widespread adoption include the need to improve their cycling lifetime, as well as stability and avoiding degradation mechanisms such as zinc dendrite growth and hydrogen-producing side reactions. X-ray computed tomography (CT) is a widely used technique for the study of batteries. In situ / operando x-ray CT has been increasingly used to study the zinc anode of zinc-air batteries to evaluate the interesting morphological changes occurring during the reaction from zinc (Zn) to zinc oxide (ZnO) during discharge (vice versa during charge). However, several studies have been carried out using synchrotron x-ray sources, which have limited availability for users. In this work, we present a comprehensive study of the discharge of commercial, primary zinc-air batteries using a laboratory-based x-ray source for in situ x-ray CT measurements. Four different discharge rates are investigated (C/30, C/60, C/90 and C/150), with tomograms collected at various stages throughout each discharge. Results confirm that with decreasing C-rate (i.e. decreasing discharge current) a greater volume of zinc is reacted, with average mass utilisations of 17%, 76%, 81% and 87% for C/30, C/60, C/90 and C/150, respectively. Furthermore, quantification using x-ray CT datasets showed that there is a direct correlation between the volume of zinc remaining in the cell and the state-of-charge of the cell, which deviated from linearity for the longer C-rates. Finally, a potential new mechanism for shape change is discussed, where a Zn particle is replaced with a pore of a similar volume. As well as improvements in statistical relevance gained from multiple repeats for each C-rate, the results presented here could be used in both modelling of battery performance, as well as consideration for future anode design concepts.

## 1. Introduction

Given the urgent need to move to low-carbon technologies, batteries are being increasingly used in a range of applications, from personal electronics to vehicles to stationary power. Lithium-ion batteries are the most widely used chemistry, but to meet the growing demand, there is a need to move beyond lithium towards alternative battery chemistries [1]. Metal–air batteries are a group of such battery alternatives that hold promise, especially for stationary power and flexible electronics applications [2]. Because oxygen from the air is the reactant on the cathode side, the theoretical specific energies of metal-air cells are significantly higher than Li-ion cells, as the reactant does not need to be stored in the battery itself [3]. Of the metal–air batteries, zinc–air cells are one of the most promising technologies. Whilst the theoretical specific energy is lower than Li–air (~1350 Wh kg<sup>-1</sup> for zinc–air, versus 5200 Wh kg<sup>-1</sup> for Li–air [2]), it is still around three times higher

than Li-ion (upwards of 270 Wh kg<sup>-1</sup> [4]) and work by Hopkins *et al* has shown that the practical specific energy of secondary cells can compete with projected values for Li–air [5], with primary zinc–air cells already reaching practical specific energies of 450 Wh kg<sub>sys</sub><sup>-1</sup>. Furthermore, significant advantages of zinc–air technologies include the ability to use aqueous electrolytes, since there are fewer safety concerns associated with the contact between zinc and water, and there is no risk of thermal runaway, explosion, or fire [6, 7]. The materials inside zinc–air cells are relatively low-cost and zinc is one of the most abundant metals in the Earth's crust [8], which makes them an attractive battery alternative as demand continues to rise. Primary zinc–air batteries are already commercialised, with wide-spread adoption for low-current, personal electronics applications, like hearing aids, but the market is growing for the use of zinc–air batteries in stationary power and large-scale storage applications [9].

Zinc–air batteries have three main components: a zinc anode, a cathode with a catalyst tailored to the oxygen reduction reaction (ORR)—or a bifunctional catalyst capable of both ORR (discharge) and oxygen evolution reaction during charge, and a separator (e.g. made from glass-fibre materials) soaked in an aqueous alkaline electrolyte, such as KOH. The cell reactions proceed as stated below, with the forward reaction in all cases being the discharge and the reverse reaction being the charge. At the anode, zinc is converted to zinc oxide (ZnO), via a zincate (Zn(OH) $_4$ <sup>2-</sup>) intermediate, which is dissolved in the electrolyte. At the cathode, oxygen from the air reacts with water via an electrochemical reduction reaction to form hydroxide. Overall, zinc is converted to ZnO during discharge and back to zinc during charge (in the case of secondary cells):

Anode: 
$$Zn + 4OH^- \rightleftharpoons [Zn(OH)_4]^{2-} + 2e^-$$
 (1)

$$\left[\operatorname{Zn}(\operatorname{OH})_{4}\right]^{2-} \rightleftharpoons \operatorname{ZnO} + \operatorname{H}_{2}\operatorname{O} + 2\operatorname{OH}^{-} \tag{2}$$

Cathode: 
$$\frac{1}{2}O_2 + H_2O + 2e^- \rightleftharpoons 2OH^-$$
 (3)

Overall: 
$$Zn + \frac{1}{2}O_2 \rightleftharpoons ZnO$$
. (4)

Widespread adoption of secondary zinc—air batteries is at present limited by insufficient bifunctional catalysts for the cathode [10–12], but there is growing interest in improving the anode architecture to help improve cycle lifetime and avoid zinc dendrite formation in both primary and secondary cells [13, 14]. Although alternative methods for recharging have been suggested, such as mechanical recharging by replacement of the anode [15] or flow-battery systems [16], challenges remain for zinc—air batteries in order to maximise the full capacity of the anode during cell discharge. Furthermore, zinc—air batteries have been shown by electrochemical impedance spectroscopy (EIS) to have a significant rate-dependence, with increasing capacity utilisation with decreasing rate (i.e. longer discharge times) [17]. However, while electrochemical methods like EIS can provide information about the bulk behaviour, they do not provide any information about anode morphology and the changes occurring within the electrode microstructure during discharge.

X-ray computed tomography (CT) is a versatile technique for imaging energy materials in three and four dimensions (three spatial dimensions plus time), and it has been widely used for imaging both energy storage and conversion technologies, like batteries and fuel cells, respectively [18]. An advantage of the technique is that it is non-destructive, meaning that the entire sample can be imaged in 3D without the need to disassemble the sample. Thus, changes in the morphology of a sample can be tracked throughout an experiment, for example, during a full discharge cycle of a battery. X-ray CT has been increasingly used for in situ and operando studies of both primary and secondary zinc-air batteries. Some of the earlier studies include work by Arlt et al to investigate the state-of-charge (SoC) in primary commercial cells and model some of the mechanisms for shape change and particle shrinking [19], and work by Schröder et al to monitor the air electrode during discharge [20]. More recent work has included the study of shape change of zinc during discharge/charge cycles [21], deposition of zincate onto the cathode [22], and morphology changes in zinc sponges during cycling [23]. Degradation mechanisms like dendrite growth have also been studied using operando x-ray CT [13] and imaging data has been used to validate models for zinc particle shape change [24]. Limitations of some of the works mentioned here are that they were carried out at synchrotron x-ray sources [13, 23]. While synchrotron sources are unmatched in terms of x-ray flux, which allows for higher temporal resolution, access to beamlines is limited and experiment durations are often short, with limited scope for replicate experiments. In contrast, laboratory-based x-ray sources are more widely available and while they are limited by flux, the spatial resolutions that can be achieved for full-field imaging are approaching those of synchrotron sources [25]. Their availability means that repeating measurements on

multiple samples is possible, which greatly improves the statistical robustness of results. Finally, very low C-rates (like the C/150 rate used in this work), which take  $\sim$ 6 d, can be investigated; such long experiments times cannot be carried out easily using synchrotron sources.

This work presents a comprehensive study of the discharge of primary, commercial zinc—air cells at different *C*-rates and correlates the electrochemical behaviour to electrode morphology changes using *in situ*, lab-based x-ray CT. We present new insights into mechanisms for shape-change during discharge, as well as providing a thorough statistical analysis by carrying out multiple repeats of experiments. Finally, we present new methods for quantifying the volume of zinc at different SoC and suggest how these methods could be applied to the design and engineering of novel anode architectures.

## 2. Experimental and methodology

#### 2.1. Electrochemical

Commercial 300 mAh PR48 hearing aid cells were used throughout this work and were discharged at various *C*-rates. A total of four cells were discharged for each *C*-rate and four different *C*-rates were investigated, namely *C*/30, *C*/60, *C*/90, and *C*/150, with *C*/30 being the highest and *C*/150 being the lowest. Thus, a total of 16 cells were discharged. For each *C*-rate, three cells were imaged at the start and end of discharge and a fourth cell was imaged at intervals throughout discharge (see section 2.2 for details of imaging), with all information about *C*-rate, corresponding discharge current, and time intervals, summarised in table 1. In this work, when a voltage of 1.1 V was reached, the cell was considered to be 'discharged' (according to the manufacturer's specifications) and full discharge data for all 16 cells can be found in (figure S1 (available online at stacks.iop.org/JPMATER/5/014001/mmedia)) of the supplementary information (SI). Given the high overpotentials in the fastest discharge measurements, the voltage limit was set slightly below 1.1 V for the cells discharged at *C*/30, as can be seen in (figure S1(a)).

## 2.2. X-ray computed tomography (x-ray CT)

X-ray CT was performed using a Nikon XT 225 (Nikon, Tring, UK). The sample was mounted inside a 3D printed jig, placed onto a sample holder and the orientation was marked on the cell as an alignment reference (figure S2(a)). Between scans, the cell was removed from the holder and discharge was continued using a potentiostat (Gamry Interface 1000, Gamry, USA), as described in the previous section. Whilst there was some minor movement in sample position arising from the removal/insertion of the cell into the holder, this was kept to a minimum using the method described above. Furthermore, during image processing, datasets were first aligned to orient the samples to identical coordinates and rotation axes.

Scans were collected with a tube voltage of 190 kV and a 0.55 mm thick copper filter was placed between the source and the sample to pre-harden the beam and minimise beam artefacts (figure S2(b)). An identical source-to-sample distance was used for each scan to keep the resolution constant (figure S2(b)), and after reconstruction with the proprietary Nikon reconstruction software CT Pro 3D (Nikon, Tring, UK), resulting images for all datasets had a voxel size of 4.91  $\mu$ m. One sample for each *C*-rate was imaged at intervals throughout the discharge (as discussed in the previous section), in addition to the 'fresh' and 'discharged' state, and three samples for each *C*-rate were imaged in the 'fresh' and 'discharged' state only. The repeats were performed to both allow better statistical analysis of the results, as well as to confirm that pausing the discharge of the *in situ* samples did not affect the discharge time of the cell. The discharge times of the *in situ* cells were found to be consistent with those discharged continuously, thus confirming that the intermittent pausing of discharge did not affect cell performance.

## 2.3. Image post-processing

Post-processing of each dataset was carried out using Avizo software (Thermo Fisher Scientific, USA). First, each sample was registered to the 'fresh' sample using the 'Register Images' module in Avizo, to ensure the orientation of each image was identical, followed by application of a median filter to reduce the noise in each tomogram. A 3D volume rendering of a cell in the 'discharged' state, which was discharged at C/90, is shown in figure 1(a) and a portion of the rendering has been removed from view such that the internal features of the cell can be visualised. The outer and inner cell casing can be seen and contain both the unreacted zinc particles and the bulk ZnO species, as well as the mesh at the bottom of the cell. An example xy orthoslice (indicated in figure 1(a)) is shown in plan-view in its original grayscale form in figure 1(b) and with the segmented phases overlaid in figure 1(c). Segmentation of the zinc phase was carried out using a thresholding approach, where a lower threshold value of  $\sim 68\%$  of the upper threshold value was chosen, with the upper threshold value being the maximum grayscale value of the dataset. This was to ensure that the relative differences in the histogram were accounted for, and the same ratio of zinc was segmented. To confirm this method, the outer cell casing was also segmented using the same approach and the volume

**Table 1.** Details of the chosen *C*-rate and discharge currents. The hours at which scans were collected for *in situ* experiments are also given.

C-rate, $C/N$ ; $N=$	Discharge current/mA	Time intervals for in situ imaging/h
30	10	0, 1, 2, 3, 4, 5
60	5.00	0, 5, 22, 28, 44
90	3.33	0, 5, 22, 28, 44, 49, 66, 71, 75
150	2.00	0, 24, 49, 74, 99, 124, 138

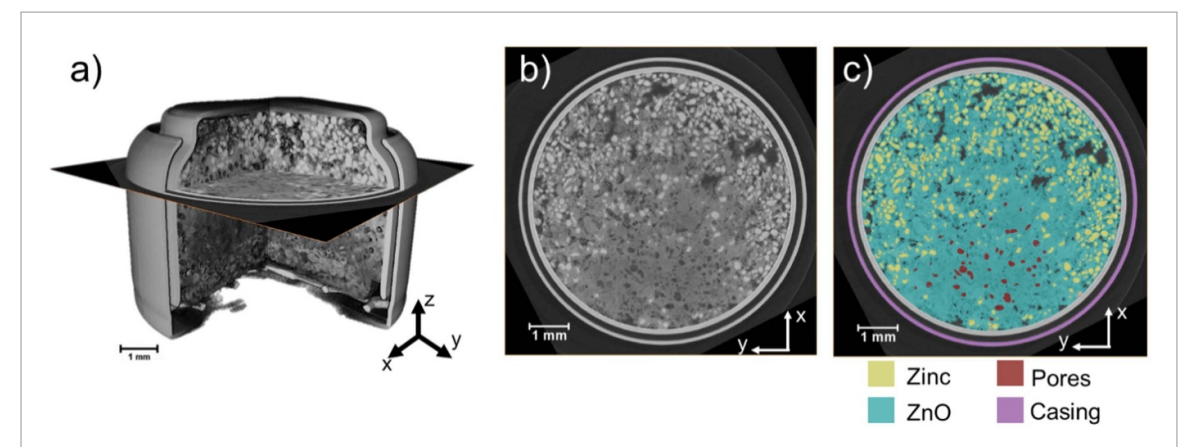


**Figure 1.** (a) Volume rendering of a cell discharged at *C*/90 in the 'discharged' state. A section of the cell has been removed from the visualisation to allow for the internal features of the cell to be displayed. The *xy* ortho-slice shown in (b) and (c) is indicated on the image. The outer cell casing can be seen, with the outer and inner casings, as well as the mesh separating anode and cathode at the bottom of the cell; (b) filtered grayscale *xy* ortho-slice, where the light grey zinc particles and casing materials are seen, as well as the dark grey zinc oxide phase and the black 'pore' phase; (c) same *xy* ortho-slice from the segmented dataset, with zinc (yellow), zinc oxide (blue), pores (red) and casing (purple).

fraction of the zinc and the outer cell casing was measured. This will be discussed further in section 3.1. A 'pore' phase was also segmented using a thresholding approach, followed by manual refinement of the thresholded values to remove any voxels assigned to regions that did not belong to the 'pore' phase (figure 1(c), red phase). This is because the grayscale values of these isolated pores that are contained within the ZnO solid phase and the values of the empty regions of the cell casing are similar. The pore phase was segmented in all 'discharged' datasets for cells discharged at rates of C/90 and C/150.

Measurement of the zinc volume fraction was carried out using the 'volume fraction' module in Avizo. The volume was then converted to a theoretical capacity, using the following equation:

$$C_{\text{segmented}} = V_{\text{segmented}} \left( \text{mm}^3 \right) \times \rho \left( \text{g mm}^{-3} \right) \times C \left( \text{mAh g}^{-1} \right)$$
 (5)

where  $C_{\text{segmented}}$  is the segmented capacity,  $V_{\text{segmented}}$  is the volume of the segmented zinc phase in mm<sup>3</sup>,  $\rho$  is the density of solid zinc in g mm<sup>-3</sup>, taken to be 0.0071 g mm<sup>-3</sup> [5], and C is the theoretical specific capacity of zinc, taken to be 825 mAh g<sup>-1</sup> [26].

Further advanced metrics for understanding changes in morphology arising from cell discharge included the calculation of the continuous particle size distribution (cPSD) for the zinc in each of the cells, then averaging over the four samples in the 'fresh' and 'discharged' state. The cPSD was calculated using an ImageJ plugin, developed by Münch *et al* [27]. Values for the average diameter of the 'pore' phase, found in cells discharged at rates of *C*-90 and *C*-150, were also calculated using the same method.

Animations of each *in situ* discharge were created using the 'Animations' tool in Avizo. Due to each dataset being aligned to the 'fresh' dataset for each *C*-rate, an identical ortho-slice in the *xz* plane was selected at each time interval for the four discharge rates. After adding scalebars and timestamp labels to each ortho-slice image, they were stitched together sequentially to create the animations. The four animations are found in the SI, for the four *in situ* measurements at different *C*-rates.

## 3. Results and discussion

## 3.1. Rate-dependency of discharge

The discharge data for each *in situ* cell discharge at the four *C*-rates are shown in figures 2(a)–(d), with the voltage spikes arising from the pause in the discharge during imaging. As can be seen in all cases, the  $\sim$ 1 h interruption did not negatively influence cell performance. Full discharge data for all four cells can be found

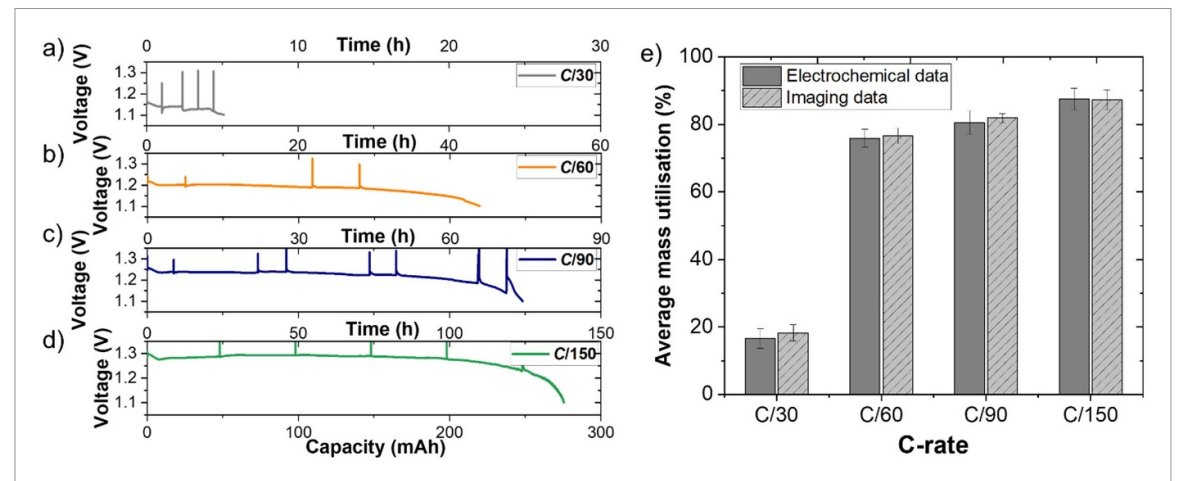


**Figure 2.** Example discharge profiles for one of the four cells for each *C*-rate; (a) *C*/30 discharge at 10 mA (grey); (b) *C*/60 discharge at 5 mA (orange); (c) *C*/90 discharge at 3.33 mA (blue) and (d) *C*/150 discharge at 2 mA (green). For each graph, the bottom *x*-axis represents the capacity (with a maximum value of 300 mAh) and the top *x*-axis represents the time of discharge, with the axis label and tick mark values shown in each case; (e) average mass utilisation (taking the average of the four cells for each *C*-rate) based on electrochemical data (dark grey bars) and imaging data (light grey bars, black diagonal lines). Error bars are also shown based on the standard deviation.

in (figure S1) of the SI. None of the cells reached full discharge of the 300 mAh capacity at 1.1 V. The poorest discharge performance was for the highest discharge rate of *C*/30 (i.e. highest current of 10 mA) (figures 2(a) and (e)). By halving the discharge current to 5 mA (*C*/60), there was a ca. 60% increase in the capacity of zinc discharged. From 5 to 3.3 to 2 mA (*C*/60 to *C*/90 to *C*/150, respectively), there were increases in the mass utilisation, from 75.8% to 80.5% to 87.4% of the 300 mAh capacity, respectively (figure 2(e), dark grey bars). Such a rate dependency has also been reported by others [17], thought to arise from increasing resistance resulting from the higher current, which leads to larger internal overpotentials. It could also be due to oxide formation effectively 'blocking' the active material at higher rates, though the exact nature of this relation is complex and dependent on many factors, like electrode thickness, particle size and/or electrolyte concentration [28]. The inability of zinc–air cells to fully discharge at a relatively high *C*-rate of *C*/30 is not yet well understood. Furthermore, when compared with typical zinc–air studies at lower *C*-rate discharges, and where only 10%–25% of the capacity is discharged [29], there still appears to be an inefficient use of battery capacity. Work in the area of improving zinc–air batteries that have faster charge/discharge capabilities and longer lifetimes is necessary.

Also shown in figure 2(e) are the values for the average percentage of zinc volume discharged based on calculations from the imaging data (light grey bars, black diagonal lines). For all *C*-rates, there is good agreement between the electrochemical and imaging data points, although the values from the imaging data are slightly higher for *C*-rates of *C*/30, *C*/60 and *C*/90, by 1.7%, 0.8%, and 1.4%, respectively. The slightly higher values imply that the segmentation has overestimated the amount of zinc discharged (i.e. the zinc volume remaining is lower than expected). However, this may be a result of some zinc being converted to zincate, dissolved in the electrolyte, and causing further reactions. The exact values for the percentages discharged are found in table 2, along with the measured zinc and casing volumes, and the average capacity (calculated from the zinc volume segmented in each of the four datasets for each *C*-rate). Firstly, looking at the 'volume' columns, the average casing volume across the 16 samples segmented is in the range of 10.1–10.4 mm<sup>3</sup>, confirming that the segmentation method used across all samples was consistent. The values for average zinc volumes in the 'fresh' and 'discharged' states were used to calculate average percentage discharge values, as well as the average capacity.

Furthermore, examining the values for capacity, for all discharge rates, the average capacity remaining is larger when calculated from the electrochemical data than when calculated from imaging data. This suggests that the volume of zinc that was segmented is smaller than expected, which further points to the fact that some zinc has dissolved in the electrolyte and is reacting, but this has not been captured by the segmentation. This phenomenon has also been suggested for other similar zinc–air cells from different manufacturers [19]. It is interesting to note that the difference between electrochemical and imaging values decreases with decreasing C-rate, from +15.8 mAh for C/30 to +5.0 and +5.3 mAh for C/60 and C/90, respectively, and to +0.5 mAh for C/150. A suggested reason for this is that the zinc either in the bulk or dissolved in the electrolyte is increasingly reacted during longer periods of discharge, meaning that the volume of zinc in the

**Table 2.** Volume and capacity data across imaging and electrochemical (EC) experiments, including standard deviation  $(\sigma)$ .

	Volume		Percentage		Capacity					
C-rate, C/N; N=	Average volume/mm $^3$ ( $\sigma$ /mm)		Average casing	Average percentage discharged/% ( $\sigma$ /%)		Difference	Average capacity remaining, imaging/mAh ( $\sigma$ /mAh)		Average capacity remaining, EC,	Difference
	Fresh	Discharged	volume/mm <sup>3</sup>	EC, $\%_E$	Imaging, $\%_I$	$(\%_E - \%_I)/\%$	Fresh	Discharged, $C_I$	$C_E/\text{mAh} (\sigma/\text{mAh})$	$C_E - C_I/\text{mAh}$
30	49.0 (0.6)	38.5 (1.7)	10.4 (0.3)	16.6 (3.0)	18.3 (2.4)	-1.7	286.8 (3.4)	225.4 (9.9)	234.4 (7.5)	+15.8
60	49.3 (0.2)	11.5 (1.2)	10.1 (0.5)	75.8 (2.7)	76.6 (2.3)	-0.8	288.6 (1.0)	67.5 (6.9)	72.5 (8.0)	+5.0
90	50.1 (1.0)	9.1 (0.8)	10.2 (0.4)	80.5 (3.5)	81.9 (1.3)	-1.4	293.2 (5.7)	53.2 (4.5)	58.5 (10.5)	+5.3
150	49.5 (1.1)	6.3 (1.5)	10.3 (0.3)	87.4 (3.1)	87.2 (2.9)	+0.2	290.2 (6.7)	37.0 (8.7)	37.5 (9.5)	+0.5

particle form is the main reacting species by the end of the discharge at *C*/150. However, further confirmation of this is needed, which may be achieved by weighing the final reaction products, for example.

## 3.2. In situ observation of discharge

The reaction from Zn to ZnO is accompanied by significant volume expansion, and with decreasing discharge current, the occupied volume of the cell casing increases, as can be seen by the transfer from light grey zinc particles in the 'fresh' cells (figures 3(a), (c), (e) and (g) for discharge rates of C/30, C/60, C/90 and C/150, respectively) to a light-grey, bulk ZnO structure occupying most of the cell casing (figures 3(c), (f), (i) and (l)). Also shown are ortho-slices taken in an intermediate state around halfway through each discharge (figures 3(b), (e), (h) and (k)), in which the majority of the volume expansion occurs in the first half of discharge, especially for the lower discharge rates of C/90 and C/150. It is noticeable from the fastest discharge rate (C/30, figure 3(b)) that the morphology has changed little during the discharge. It appears there is a vacancy in the centre of the cell, but it is unknown what occupies this space; it could arise from hydrogen gas formation as a result of side reactions [30], but further investigation is needed to confirm this since it was not observed for discharge at lower currents.

A more detailed analysis of the discharge is afforded by observing the changes in morphology as it proceeds, which can be seen in the accompanying animations for the *in situ* discharge at each *C*-rate (found in the SI). An identical ortho-slice is selected in each case and the evolution of the morphology can be tracked in each animation. The main morphology changes that were found to occur include the gradual shrinking of some zinc particles, accompanied by the formation of a less-dense, ZnO bulk material. This is consistent with the findings of Arlt *et al* who found a similar volume expansion when studying one discharge rate of a different commercial cell of type ZA13 [19]. The ZnO can also be seen to have a grayscale gradient, with dark-grey ZnO bulk at the top with decreasing grayscale values towards the separator. This implies that even though the reaction appears to occur from the regions closest to the separator first, as discussed by Arlt *et al* [19], the volume expansion effectively pushes the zinc further away from the separator, meaning that more zinc is concentrated in the top part of the cell. This effect is more prevalent in the longer discharge rates (*C*/90 and *C*/150), where any unreacted zinc that is likely not in particle form and is in the lower regions near the separator gradually reacts with increasing discharge times.

As well as qualitative descriptions of morphology evolution during discharge, a quantitative analysis of the changes in the zinc volume during discharge was carried out. The *in situ* values for the measured volumes are shown in figure 3(m) for the various C-rates. As expected, with increasing time, the volume of zinc decreases approximately linearly, as would be expected from the following relation (a full derivation of this can be found in equations (S1)–(S4) of the SI):

$$V_{\rm disch} = \frac{It}{\rho C} + V_{\rm initial} : V_{\rm disch} \propto t$$
 (6)

where  $V_{\rm disch}$  is the volume of zinc (mm³), I is the discharge current (mA), t is the time (h),  $\rho$  is the density of zinc (g mm³), C is the theoretical specific capacity of zinc (mAh g¹) and  $V_{\rm initial}$  is the initial volume of zinc in the cell (mm³) (equal to the y-intercept in the linear equation). The theoretical values for zinc volume, calculated by substitution into equation (6), are also shown as solid, continuous lines in figure 3(m). For all C-rates, it can be seen that the zinc volume measured from x-ray CT is lower than the theoretical volume and this becomes more pronounced with increasing length of discharge. However, even for C/90 and C/150, which appear to deviate the most from the theoretical volume, the experimental values approach the theoretical values towards the end of discharge, i.e. around 75 h for C/90 and 135 h for C/150. This implies that the discharge behaviour, as determined from the zinc volume in particle form alone, is non-linear.

To further assess the linearity of the experimental volume decrease, linear regression fits were done for all plots, with the adjusted  $R^2$  values shown in table 3 (plots of the linear regression are found in figure S3 of the SI). The C/60 and C/90 lines have very good linear fits, with values of 0.97 and 0.98, respectively. On the other hand, the C/30 and C/150 fits have values of 0.94 and 0.93, respectively, which indicates that they deviate significantly from linearity. This can be seen by eye in figure 3(m) (and figure S3), especially for the C/150 discharge, where the green triangles tend towards a curved rather than linear relationship. However, due to the lack of chemical information available from x-ray CT data, it is unknown whether there are still small amounts of zinc reacting that are not present in the particle form, and that may not have been picked up by segmentation. Nonetheless, the results highlight that x-ray CT is a useful tool for correlating the SoC to the volume of zinc inside the cell at different C-rates.

#### 3.2.1. Changes in particle size

The average particle diameter of the segmented zinc particles in the 'fresh' and 'discharged' states were calculated using cPSD measurement, with results shown in table 4. In the 'fresh' state, the average particle

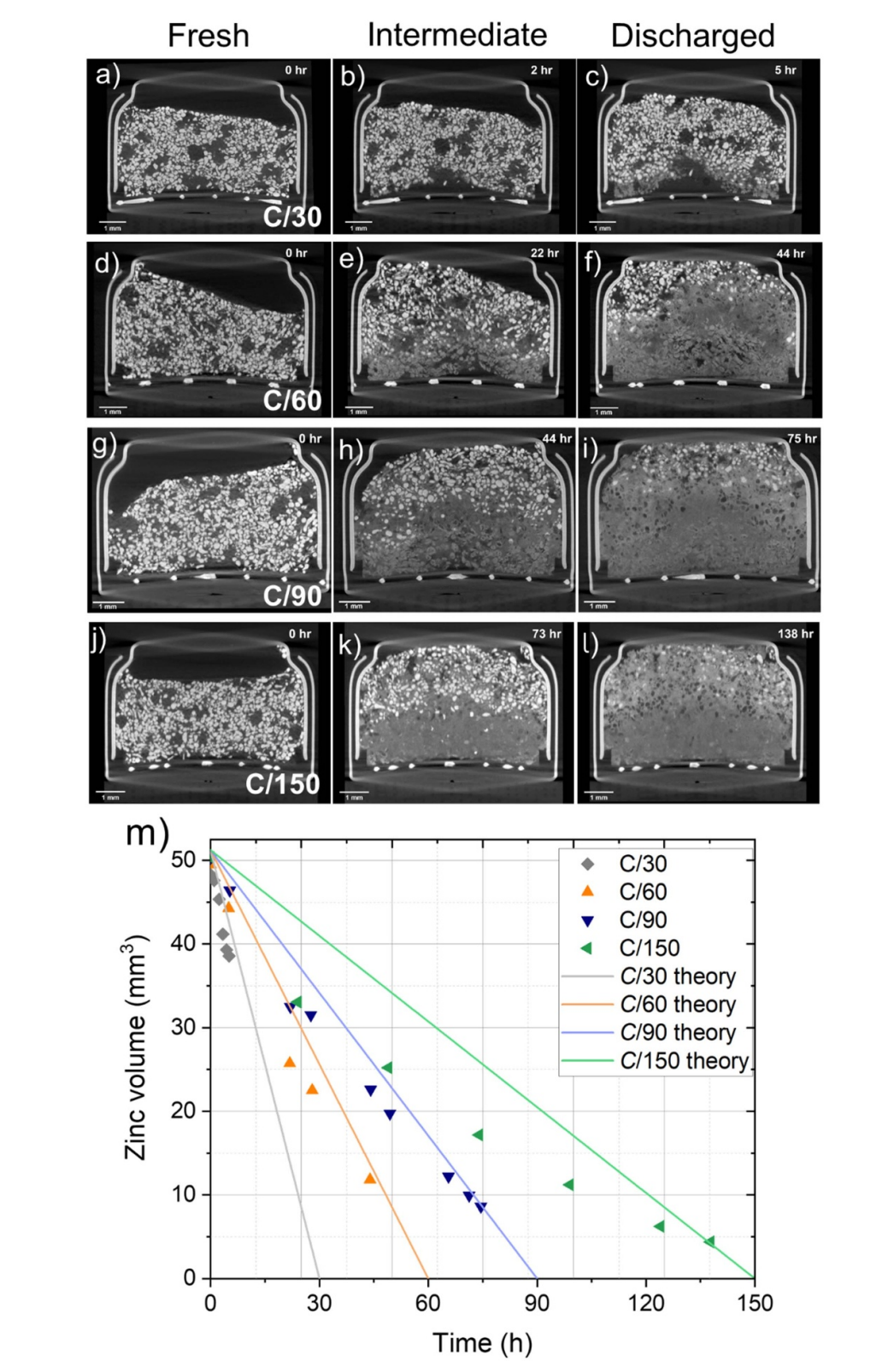


Figure 3. (a)—(l) Virtual ortho-slices taken from cells in the 'fresh' (left column), an 'intermediate' (middle column) and 'discharged' state for the C-rates C/30 (a)—(c), C/60 (d)—(f), C/90 (g)—(i) and C/150 (j)—(l); (m) graph showing the volume measured from image analysis for C/30 (grey), C/60 (orange), C/90 (blue) and C/150 (green). The theoretical volume change is also shown as solid lines in lighter, corresponding colours for each C-rate, based on equation (6).

size ranges between 112  $\pm$  4 and 114  $\pm$  1  $\mu$ m, which highlights that the segmentation has been consistent across all 16 cells. In the 'discharged' state, the average particle diameters are less consistent, with the values for C/90 (89  $\pm$  5  $\mu$ m) and C/150 (90  $\pm$  1  $\mu$ m) being lower than the values for C/60 (98  $\pm$  4  $\mu$ m) and C/30 (103  $\pm$  5  $\mu$ m). This suggests that for higher C-rates (i.e. C/30 and C/60), more full particles have disappeared, but at lower C/rates (C/90 and C/150) there is increased particle shrinkage along with the

**Table 3.** Table showing the adjusted  $R^2$  values for the decreasing zinc volume at the various C-rates.

$\overline{C}$ -rate, $C/N$ ; $N=$	Adjusted R <sup>2</sup> value
30	0.95
60	0.97
90	0.98
150	0.93

**Table 4.** Average particle sizes, calculated by cPSD, in the 'fresh' and 'discharged' state for the various *C*-rates of interest, along with the average pore diameter in the 'discharged' state.

C-rate, $C/N$ ; $N=$	Average fresh particle diameter, $d_{\text{Fresh}}/\mu\text{m}~(\sigma/\mu\text{m})$	Average discharged particle diameter, $d_{\rm Disch}/\mu{\rm m}~(\sigma/\mu{\rm m})$	Average pore diameter, $d_{ m pore}/\mu{ m m}~(\sigma/\mu{ m m})$
30	112 (4)	103 (5)	_
60	114 (1)	98 (4)	<del></del>
90	113 (2)	89 (5)	79 (2)
150	114 (2)	90 (1)	86 (4)

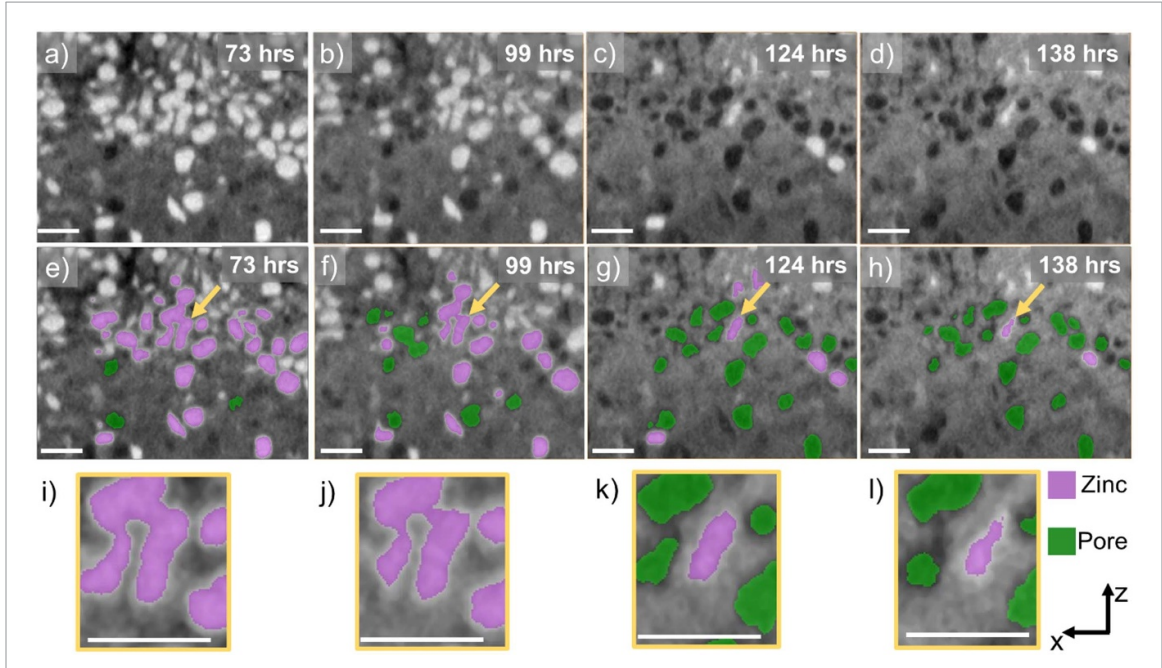


**Figure 4.** (a)–(d) Example region from the latter stages of cell discharge at a rate of C/150 (2 mA), with increasing time ((a)–(d), 73, 99, 124 and 138 h, respectively); (e)–(h) the same region with a number of example zinc particles highlighted in pink and pores emphasised in green, showing how the zinc particles transform into pores; (i)–(l) expanded view of an example zinc particle that shrinks during discharge (also indicated by yellow arrows in (a)–(d); (e)–(h) represents 73, 99, 124 and 138 h, respectively). Scalebars represent 300  $\mu$ m in all cases.

disappearance of particles. The increasing thickness of the oxide layer between the separator and the remaining zinc particles at lower C-rates could also play a role in this. Furthermore, whilst the average particle diameter decreased in all cases, the decrease is only between 9 and 24  $\mu$ m (8% and 21% decrease of diameter, respectively). These values are not as large as might be expected, given the volume of zinc that is converted to zinc oxide. This indicates that the mechanism for conversion from zinc particle to ZnO bulk phase occurs relatively quickly and on a few particles at a time located nearer to the separator, as opposed to a gradual shrinking of all particles simultaneously.

Further evidence for this hypothesis is suggested by the presence of pores in the 'discharged' state volumes, as shown in figure 4, especially for longer discharge rates. Such pores are not seen in the cells discharged at *C*/30 and there are fewer in the cells discharged at *C*/60, only first being detected in the final images. However, for the cells discharged at *C*/90 and *C*/150, the pores are found in increasing numbers after 49 and 73 h, respectively, corresponding to 65% and 52% through the discharge. A suggested reason for this is that the pores only begin to form once the empty volume inside the anode casing is sufficiently filled by the expanding reacted ZnO (and remaining zinc), which occurs roughly 50%–65% through the discharge.

To investigate the morphology of the pores, a 'pore' phase was segmented in the 'discharged' dataset of all cells at C/90 and C/150 and the average value was calculated (table 4). Average pore diameter values were found to be  $79 \pm 2~\mu m$  and  $86 \pm 4~\mu m$  for the C/90 and C/150 cells, respectively. Interestingly, these pore diameters are similar to the values of discharged zinc, 89 and 90  $\mu m$  for C/90 and C/150, respectively, albeit slightly smaller. However, the similarity in values still presents strong evidence for the fact that at some stage in the discharge, the zinc particles have disappeared, but do not affect the local morphology.

The formation of pores over a discharge can also be seen by comparing an identical region in x-ray CT datasets, as shown in figures 4(a)–(d), for the cell discharged at 2 mA (C/150) with *in situ* collection of images. Example particles and pores (pink and green, respectively) are overlaid onto the same images to emphasise this change and shown in figures 4(e)–(h). Whilst there are a few pores present already in the scan at 73 h (figures 4(a)–(e)), as indicated in green, subsequent images show how the majority of the light grey, zinc particles (pink) are converted to pores (green) in almost identical locations (figures 4(b)–(d)/(f)–(h)). As well as pore formation, some zinc particles can be seen to shrink during the discharge (but are not converted into pores), such as the particle indicated by the yellow arrow in the images in figures 4(e)–(h) and shown in an expanded view in figures 4(i)–(l). Further investigation of this phenomenon should be done by collecting multiple scans with shorter time frames (for example, every hour) towards the end of cell discharge, to elucidate the mechanism for pore formation.

Because chemical information cannot be obtained from conventional absorption x-ray CT images, it is not possible to determine whether these 'pores' are due to an absence of material, or whether there is a separate low-density solid phase occupying them. Thus, a future investigation could make use of either x-ray photoelectron spectroscopy (XPS) or x-ray diffraction (XRD) methods to provide further insight into the chemical nature of these pores. Nonetheless, the presence of a pore phase could potentially be utilised in the future design of rechargeable zinc—air cells; for example, such pores could act like a scaffold, or as nucleation points, into which ZnO could form. Such scaffolds have been suggested in the form of sponges [23, 31], and it is clear to see here that they could play a significant role in increasing the lifetime of rechargeable zinc—air batteries.

## 4. Conclusion

This work has presented an in-depth, rigorous study of 300 mAh commercial zinc—air primary cells discharged at various *C*-rates. The electrochemical discharge profiles were correlated to the cell morphology by analysis of tomograms obtained by lab-based x-ray CT. The rates investigated were *C*/30, *C*/60, *C*/90 and *C*/150, corresponding to discharge currents of 10, 5, 3.3 and 2 mA, respectively. Results showed that decreasing the discharge current increased the utilised capacity of the cell, up to an average of 87.4% for the *C*/150 discharge. Segmentation of zinc from 3D imaging datasets showed that the volume of zinc particles remaining in the cell could be correlated to the SoC of the cell. *in situ* datasets showed that the decrease in zinc volume across discharge at all *C*-rates was approximately linear for the higher *C*-rates of *C*/30 and *C*/60, but deviated from linearity for *C*/90 and, particularly, *C*/150.

Analysis of the zinc particle diameters showed that there was a reduction in the average particle size between the 'fresh' and 'discharged' state for all C-rates, with little difference between the longest discharge times of 89  $\mu$ m for C/90 and 90  $\mu$ m for C/150. The particle shrinking is accompanied by a volume expansion in all cases, but the least volume expansion occurs for the highest discharge current of C/30. Furthermore, in all cases, zinc reacted from the 'bottom' of the cell, i.e. closest to the cathode and separator first, resulting in the movement of zinc particles away from the separator as the Zn to ZnO reaction occurred. Investigation of the morphology using in situ x-ray CT showed that pores form during discharge at lower C-rates, which had average diameters similar to the average zinc particle diameter. The suggested reason is that once the solid volume expansion has filled a significant volume inside the anode casing, the zinc particles can no longer react via the previously known shrinking-core model, and instead proceed via a different mechanism, which is not yet well-understood. Taking more scans in the later stages of discharge, or by carrying out other characterisation techniques, like XRD or XPS, may present and additional beneficial investigation to understand this secondary mechanism.

In summary, we have shown evidence for a different reaction mechanism in the latter stages of discharge, as well as highlighting that the zinc volume can be correlated to *C*-rate. We anticipate that these results provide good foundations for the creation of future models and will lead to improved anode morphologies and designs. Finally, by using widely available lab-based x-ray CT, we have shown that lab-based x-ray sources hold great potential for producing high-quality datasets with repeatable results for future investigation of emerging zinc—air electrode architectures.

## Data availability statement

The data that support the findings of this study are available upon reasonable request from the authors.

## Acknowledgments

This work was supported by the Engineering and Physical Sciences Research Council (EPSRC) (EP/R023581/1, EP/M028100/1, EP/S018204/2) and Faraday Institution (Faraday.ac.uk; EP/S003053/1, Grant Nos. FIRG013 and FIRG015). J H acknowledges the EPSRC for supporting her Doctoral Prize Fellowship (EP/T517793/1). PRS acknowledges the support of The Royal Academy of Engineering (CiET1718/59) and D B was supported by the Royal Academy of Engineering under the Research Chairs and Senior Research Fellowships scheme.

## **ORCID** iDs

Jennifer Hack https://orcid.org/0000-0002-5529-4750

Drasti Patel https://orcid.org/0000-0003-4288-2825

Josh J Bailey https://orcid.org/0000-0003-2397-6690

Francesco Iacoviello https://orcid.org/0000-0003-3564-2380

Paul R Shearing https://orcid.org/0000-0002-1387-9531

Dan J L Brett https://orcid.org/0000-0002-8545-3126

## References

- [1] Luntz A 2015 Beyond lithium ion batteries J. Phys. Chem. Lett. 6 300–1
- [2] Rahman M A, Wang X and Wen C 2013 High energy density metal-air batteries: a review J. Electrochem. Soc. 160 A1759-71
- [3] Lee J-S, Tai Kim S, Cao R, Choi N-S, Liu M, Lee K T and Cho J 2011 Metal-air batteries with high energy density: Li-air versus Zn-air Adv. Energy Mater. 1 34–50
- [4] Eftekhari A 2019 On the theoretical capacity/energy of lithium batteries and their counterparts ACS Sustain. Chem. Eng. 7 3684–7
- [5] Hopkins B J, Chervin C N, Long J W, Rolison D R and Parker J F 2020 Projecting the specific energy of rechargeable zinc-air batteries ACS Energy Lett. 5 3405–8
- [6] Sharma S, Anand A, Shukla A and Sharma A 2020 Safety and environmental impacts of Zn batteries Zinc Batteries (New York: Wiley) pp 131–50
- [7] Larsson F, Rytinki A, Ahmed I, Albinsson I and Mellander B-E 2017 Overcurrent abuse of primary prismatic zinc–air battery cells studying air supply effects on performance and safety shut-down *Batteries 3* 1
- [8] Hopkins B J, Chervin C N, Sassin M B, Long J W, Rolison D R and Parker J F 2020 Low-cost green synthesis of zinc sponge for rechargeable, sustainable batteries Sustain. Energy Fuels 4 3363–9
- [9] Fu J, Cano Z P, Park M G, Yu A, Fowler M and Chen Z 2017 Electrically rechargeable zinc–air batteries: progress, challenges, and perspectives *Adv. Mater.* 29 1604685
- [10] Zhang J, Zhou Q, Tang Y, Zhang L and Li Y 2019 Zinc-air batteries: are they ready for prime time? Chem. Sci. 10 8924-9
- [11] Li J, Meng Z, Brett D J L, Shearing P R, Skipper N T, Parkin I P and Gadipelli S 2020 High-performance zinc-air batteries with scalable metal-organic frameworks and platinum carbon black bifunctional catalysts ACS Appl. Mater. Interfaces 12 42696–703
- [12] Li Y, Gong M, Liang Y, Feng J, Kim J-E, Wang H, Hong G, Zhang B and Dai H 2013 Advanced zinc-air batteries based on high-performance hybrid electrocatalysts *Nat. Commun.* 4 1805
- [13] Yufit V, Tariq F, Eastwood D S, Biton M, Wu B, Lee P D and Brandon N P 2019 *Operando* visualization and multi-scale tomography studies of dendrite formation and dissolution in zinc batteries *Joule* 3 485–502
- [14] Wang K, Pei P, Ma Z, Chen H, Xu H, Chen D and Wang X 2015 Dendrite growth in the recharging process of zinc–air batteries *J. Mater. Chem.* A 3 22648–55
- [15] Singh S K, Dhavale V M and Kurungot S 2015 Surface-tuned Co<sub>3</sub>O<sub>4</sub> nanoparticles dispersed on nitrogen-doped graphene as an efficient cathode electrocatalyst for mechanical rechargeable zinc—air battery application ACS Appl. Mater. Interfaces 7 21138–49
- [16] Abbasi A, Hosseini S, Somwangthanaroj A, Cheacharoen R, Olaru S and Kheawhom S 2020 Discharge profile of a zinc-air flow battery at various electrolyte flow rates and discharge currents Sci. Data 7 196
- [17] Franke-Lang R and Kowal J 2021 Analysis of electrochemical impedance spectroscopy on zinc-air batteries using the distribution of relaxation times Batteries 7 56
- [18] Heenan T M M, Tan C, Hack J, Brett D J L and Shearing P R 2019 Developments in x-ray tomography characterization for electrochemical devices *Mater. Today* 31 69–85
- [19] Arlt T, Schröder D, Krewer U and Manke I 2014 In operando monitoring of the state of charge and species distribution in zinc air batteries using x-ray tomography and model-based simulations Phys. Chem. Chem. Phys. 16 22273–80
- [20] Schröder D, Arlt T, Krewer U and Manke I 2014 Analyzing transport paths in the air electrode of a zinc air battery using x-ray tomography Electrochem. Commun. 40 88–91
- [21] Christensen M K, Mathiesen J K, Simonsen S B and Norby P 2019 Transformation and migration in secondary zinc—air batteries studied by in situ synchrotron x-ray diffraction and x-ray tomography J. Mater. Chem. A 7 6459–66
- [22] Franke-Lang R, Arlt T, Manke I and Kowal J 2017 X-ray tomography as a powerful method for zinc-air battery research J. Power Sources. 370 45–51
- [23] Bozzini B, Mele C, Veneziano A, Sodini N, Lanzafame G, Taurino A and Mancini L 2020 Morphological evolution of Zn-sponge electrodes monitored by *in situ* x-ray computed microtomography ACS Appl. Energy Mater. 3 4931–40

- [24] Schmitt T, Arlt T, Manke I, Latz A and Horstmann B 2019 Zinc electrode shape-change in secondary air batteries: a 2D modeling approach *J. Power Sources.* 432 119–32
- [25] Withers P J, Bouman C, Carmignato S, Cnudde V, Grimaldi D, Hagen C K, Maire E, Manley M, Du Plessis A and Stock S R 2021 X-ray computed tomography *Nat. Rev. Methods Prim.* 1 18
- [26] Bonino F and Vincent C A 1997 Secondary alkaline cells *Mod. Batter*. ed C A Vincent, B B T-M B and S E Scrosati (Amsterdam: Elsevier) pp 162–97
- [27] Münch B and Holzer L 2008 Contradicting geometrical concepts in pore size analysis attained with electron microscopy and mercury intrusion J. Am. Ceram. Soc. 91 4059–67
- [28] Tian R, Park S-H, King P J, Cunningham G, Coelho J, Nicolosi V and Coleman J N 2019 Quantifying the factors limiting rate performance in battery electrodes *Nat. Commun.* 10 1933
- [29] Parker J F, Ko J S, Rolison D R and Long J W 2018 Translating materials-level performance into device-relevant metrics for zinc-based batteries *Joule* 2 2519–27
- [30] Lei L, Sun Y, Wang X, Jiang Y and Li J 2020 Strategies to enhance corrosion resistance of Zn electrodes for next generation batteries Front. Mater. 7 96
- [31] Parker J F, Nelson E S, Wattendorf M D, Chervin C N, Long J W and Rolison D R 2014 Retaining the 3D framework of zinc sponge anodes upon deep discharge in Zn–air cells ACS Appl. Mater. Interfaces 6 19471–6